https://doi.org/10.5194/egusphere-2026-4228
Preprint. Discussion started: 28 July 2026

Analysis of the Composition and Direct Radiative Effects of Polluted Dust Using Satellite Observations and Reanalysis Data

Ronghao Wang[1], Jianyu Zheng[2,3], Qianqian Song[1,2] Huisheng Bian[2,3], Hongbin Yu[3], and Zhibo Zhang[1,2,4],

[1]Physics Department, University of Maryland Baltimore County (UMBC), Baltimore, Maryland, USA.
[2]Goddard Earth Sciences Technology and Research (GESTAR) II, UMBC, Baltimore, Maryland, USA.
[3]NASA Goddard Space Flight Center, Greenbelt, MD, USA.
[4]Goddard Planetary and Heliophysics Institute (GPHI), UMBC, Baltimore, Maryland, USA.

Correspondence to: Zhibo Zhang (zhibo.zhang@umbc.edu)

Abstract. Mineral dust particles influence the global energy budget through interactions with both solar and terrestrial radiation. During long-range transport, dust can be not only externally but also internally mixed with local pollutant aerosols such as sulfate, nitrate, organic carbon, and black carbon. These physical and chemical interactions alter the optical properties of the resulting polluted dust particles, which remain a major source of uncertainty in computing the dust direct radiative effect (DRE). This study aims to quantify how pollution influences the shortwave and longwave optical properties and the direct radiative effects of dust aerosols using observational and reanalysis data. Following previous studies, a concentric spherical core-shell model is adopted to simulate the mixing state of dust-sulfate mixtures. In the urban environment, the pollutants such as sulfate and nitrate mainly originate from industrial activities. In the shortwave region, internal mixing of dust and pollution reduces the atmospheric reflectance, increases radiative absorption, resulting in a weaker enhancement of optical depth than that of external mixing. In the longwave region, internal mixing absorbs more radiation than external mixing, resulting in a stronger positive DRE. The study highlights the need for improved representation of dust–pollution mixing in climate models.

1 Introduction

Mineral dust is one of the most abundant aerosol types globally, accounting for a substantial fraction of the total aerosol loading (Knippertz and Stuut, 2014; Froyd et al., 2019). By scattering and absorbing both the incoming solar radiation and outgoing terrestrial radiation, dust exerts a complex direct radiative effect (DRE) that includes generally cooling effects in the shortwave (SW) spectrum and warming effects in the longwave (LW) spectrum (Yu et al., 2006; Kok et al., 2023; Song et al., 2018; Song et al., 2022; Li et al., 2025). The overall impact of dust on the Earth's radiation budget thus depends sensitively on its optical properties, which are in turn influenced by dust mineral composition, size, shape, and mixing state – i.e. whether dust particles are externally mixed (physically separate) or internally mixed (coated or dispersed structure) with other aerosols(Taylor et al.,

https://doi.org/10.5194/egusphere-2026-4228
Preprint. Discussion started: 28 July 2026

2015; Li et al., 2016; Tian et al., 2018; Song et al., 2022). Recent assessments have highlighted that accurately quantifying aerosol mixing state remains a major challenge and source of uncertainty in estimating aerosol radiative forcing (IPCC, 2021).

This study focuses on "polluted dust", i.e., the mixture of long-range transported dust aerosol with the local pollutions, e.g., acidic sulfates, nitrates, and combustion aerosols. This phenomenon has been investigated in several previous studies using different observations and from different perspectives (Cwiertny et al., 2008; Li and Shao, 2009; Hand et al., 2010; Soussé Villa et al., 2025). Laboratory studies and field observations have provided fundamental insights into the physicochemical processes of polluted dust formation: Cwiertny et al. (2008) provided a mechanistic basis for polluted dust formation through laboratory studies, showing that heterogeneous reactions of mineral dust with trace gases such as HNO_3, SO_2, and NO_2 produce deliquescent coatings that fundamentally alter the physicochemical properties of dust particles. Li and Shao (2009) provided direct ground-based evidence from haze episodes in northern China, where approximately 90% of mineral dust particles were found to be coated, predominantly with nitrate compounds. These hygroscopic coatings rendered the particles more spherical and larger, thereby enhancing their light scattering efficiency and cloud condensation nuclei (CCN) activity, collectively contributing to significant modifications in both the radiative and cloud-forming properties of dust. Similarly, Hand et al. (2010) provided in-situ airborne evidence over West Africa that biomass burning aerosols and mineral dust can occur in both externally and internally mixed states. Their single-particle ESEM-EDX analysis showed that 21%–33% of soot particles in the samples were internally associated with dust particles, suggesting that atmospheric aging processes promote internal mixing that enhances aerosol absorption and reduces single-scattering albedo.

These laboratory and field studies are limited by small size of samples, restricted spatial and temporal coverage, and lack of statistical representativeness, making it challenging to characterize the large-scale distribution of polluted dust. Satellite-based observations from the space-borne Cloud-Aerosol Lidar with Orthogonal Polarization (CALIOP) onboard the CALIPSO satellite have helped bridge this gap. Xu et al. (2023) analyzed 14 years of CALIOP data over China and surrounding areas, revealing that polluted dust is not an episodic phenomenon but a persistent and widespread feature of the regional atmosphere, with pronounced hotspots over the North China Plain, the Sichuan Basin, and the Indo-Gangetic Plain. Polluted dust was found to be largely confined in the planetary boundary layer, with maximum loading in winter due to suppressed boundary layer mixing. This underscores that dust–pollution interactions are a climatologically significant and recurrent process with substantially varying spatial patterns depending on dust source proximity, pollutant source distributions, and the prevailing meteorological conditions. Beyond East Asia, satellite observations have revealed similarly organized polluted dust distributions in other major transport corridors. Adams et al. (2012) used CALIOP-derived three-dimensional occurrence frequencies to show that polluted dust is a large-scale, seasonally varying aerosol type over the Atlantic sector, with maximum occurrence near the ITCZ where Saharan dust converges with biomass burning aerosols from equatorial Africa, highlighting the importance of large-scale atmospheric circulations in controlling dust–pollution interactions. However, a major limitation of these satellite-based studies is that remote sensing observations cannot resolve whether dust and pollutants are externally or internally mixed, nor can they specify the chemical nature of the mixed pollutants.

https://doi.org/10.5194/egusphere-2026-4228
Preprint. Discussion started: 28 July 2026

Previous studies have suggested that changes in particle composition and mixing state can substantially modify aerosol optical properties and, therefore, the direct radiative effects of dust (Li and Shao, 2009; Hand et al., 2010; Teri et al., 2025). In particular, Zhang et al. (2024) showed from a theoretical perspective that externally mixed dust–sulfate aerosols and internally mixed sulfate-coated dust can produce markedly different shortwave and longwave direct radiative effects. This highlights the need to better constrain the composition and mixing characteristics of polluted dust. However, two major gaps remain: previous studies have not systematically identified what types of pollution aerosols are mixed with transported dust in different polluted dust hotspots, nor have they sufficiently constrained how external versus internal mixing modifies the shortwave and longwave direct radiative effects of polluted dust. Inspired by Zhang et al. (2024), we use the combination of satellite observations and reanalysis data to address two important questions: 1) What kinds of pollution aerosols are mixed with transported dust in different polluted dust hotspots? 2) How does the mixing state of polluted dust, external vs. internal mixing, affect the radiative effects of dust aerosols? This study aims to bridge these gaps by combining satellite observations, reanalysis data, and theoretical modelling to assess the impacts of mixing states on polluted dust aerosol behavior. First, using 17 years of CALIOP/CALIPSO satellite lidar data (2007–2023), we identify global "hotspots" where polluted dust occurs most frequently, and we examine how these regions correspond to dust transport pathways and pollution source areas. We then use the MERRA-2 reanalysis (2007–2023) to characterize the typical aerosol composition in those polluted dust hotspots – quantifying the seasonal co-variations of dust and major pollutants (sulfate, organic carbon, black carbon, sea salt). Finally, we perform idealized radiative transfer experiments using a core–shell Mie scattering framework, which provides a physically realistic representation of the sulfate coatings frequently observed on aged mineral dust, to quantify how different dust–sulfate mixing states alter dust optical properties and direct radiative effects in both the shortwave and longwave spectra. Although our analysis is global in scope, we place particular focus on East Asia (specifically, the Capital Region of China) as a case study, since it is a prominent polluted dust hotspot where heavy industrial pollution and seasonal dust outbreaks coincide. Through this combined approach, we highlight the potential importance of representing internal mixing in aerosol models and demonstrate how assuming dust and pollution are externally mixed (as is commonly assumed in current models) could misrepresent the climate effects of dust, especially its longwave warming contribution. The findings are relevant for improving aerosol–climate models and assessments of dust's radiative forcing in polluted regions.

2 Hotspots of polluted dust revealed by CALIOP observations

2.1 Cloud-Aerosol Lidar with Orthogonal Polarization (CALIOP)

The Cloud-Aerosol Lidar with Orthogonal Polarization (CALIOP) provides continuous, multi-year global observations of clouds and aerosols by measuring vertically resolved backscatter and polarization signals. CALIOP classifies aerosol layers into subtypes using a decision-tree algorithm that combines the 532 nm integrated attenuated backscatter, the volume depolarization ratio, and surface type. Layers with estimated particulate depolarization ratios between 0.075 and 0.20 are generally classified as polluted dust. In addition, layers with depolarization ratios of 0.075 or lower may also be classified as polluted dust when they occur over desert surfaces and have a 532 nm integrated attenuated backscatter below 0.0005 sr^{-1},

https://doi.org/10.5194/egusphere-2026-4228
Preprint. Discussion started: 28 July 2026

rather than being classified as polluted continental or smoke (Omar et al., 2009; Kim et al., 2018). In this study, we use the version 4.51 (V4-51) CALIPSO Level 2 5-km merged cloud–aerosol layer product (CAL_LID_L2_05kmMLay-Standard-V4-51), which provides layer-by-layer aerosol subtype flags, vertical distribution, and optical properties of all detected cloud and aerosol layers along the CALIOP track at 5 km horizontal resolution.

To identify the major polluted dust hotspot regions globally, we analyze data from January 2007 to December 2023 and retain only nighttime, cloud-free profiles to maximize the lidar signal-to-noise ratio and minimize potential misclassification associated with nearby clouds.

2.2 Hotspot analysis of high-frequency polluted dust events

As shown in Figure 1, CALIOP observations reveal a pronounced seasonal variability in the spatial distribution of both pure dust and polluted dust during 2007–2023. For each 1° × 1° grid cell and season, the occurrence frequency of a target aerosol type, either pure dust or polluted dust, is defined as the ratio between the number of cloud-free nighttime CALIOP profiles that contain at least one layer classified as that type and the total number of cloud-free nighttime profiles in that grid cell over 2007–2023. Black "+" symbols mark grid cells where the target aerosol type accounts for more than 60 % of all cloud-free nighttime aerosol-containing profiles, indicating regions where pure dust or polluted dust dominates the aerosol column. ERA5 850-hPa winds are superimposed to highlight the large-scale transport pathways that connect dust source regions to downwind polluted environments.

As shown in Figure 1, pure dust exhibits high occurrence frequencies mainly over Northern Hemisphere desert source regions and their immediate outflow corridors. In contrast, polluted dust occurs most frequently in downwind regions under the prevailing 850 hPa circulation, where intense dust transport intersects local anthropogenic or biomass burning pollution. Polluted dust exhibits pronounced seasonal variability, with three persistent hotspots emerging in the long-term DJF climatology based on their high occurrence frequencies and large fractions relative to all aerosol types: West Central Africa (6°N–9°N, 15°W–0°W), the Indian Subcontinent (18°N–26°N, 70°E–85°E), and the Capital Region of China (36°N–40°N, 110°E–117°E). Although relatively high-polluted dust occurrence and fractions are also found in several other regions, such as the northern Central Asia and the southern United States, these regions are characterized by comparatively low dust AOD, unlike the three hotspots where polluted dust occurrence coincides with substantial dust loading (Figures S1–S5). Accordingly, these regions are not considered primary hotspots of interest in the present analysis. The three selected hotspot regions are outlined by black boxes in Figure 1 and are the focus of the subsequent analysis.

https://doi.org/10.5194/egusphere-2026-4228
Preprint. Discussion started: 28 July 2026

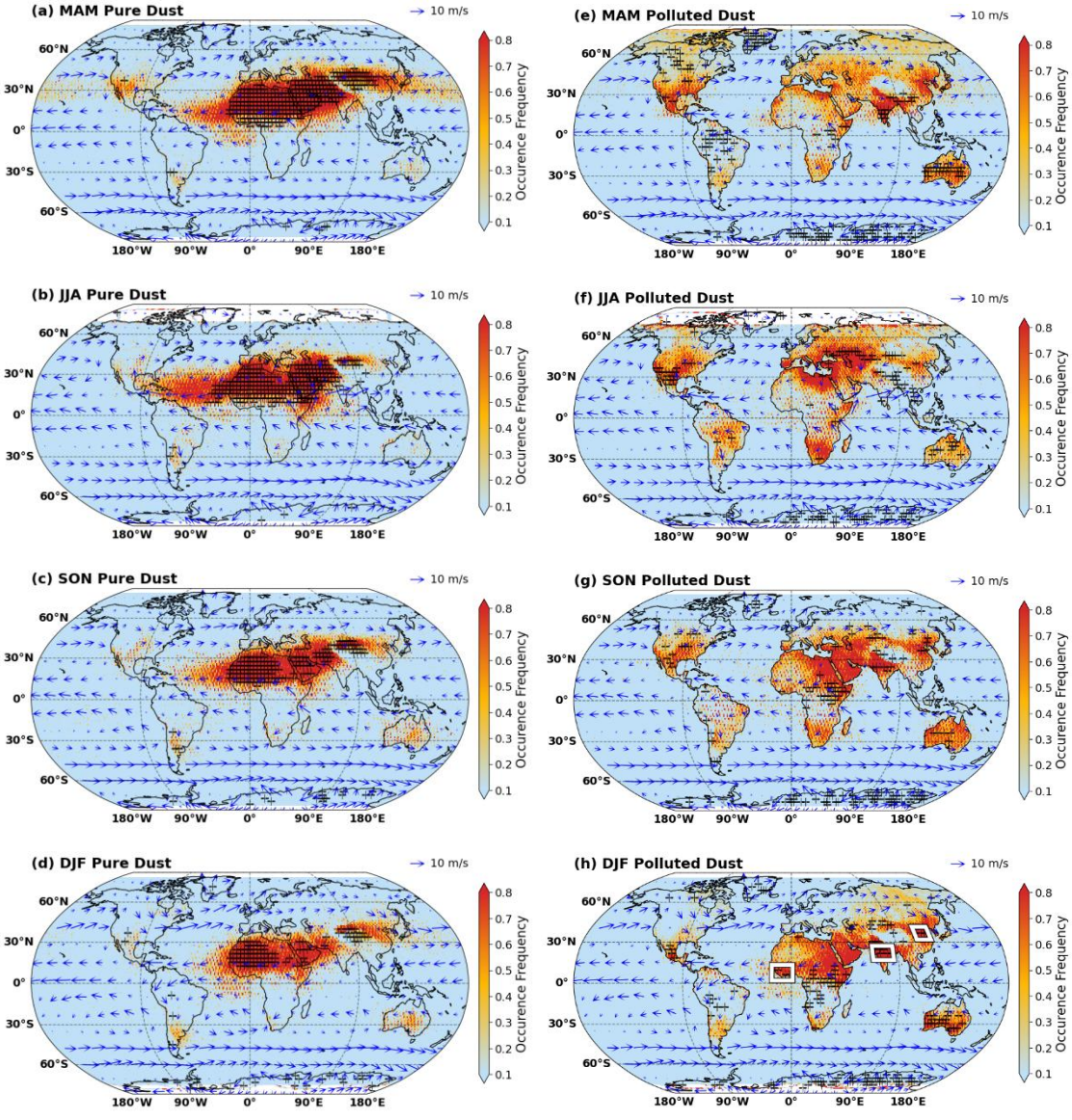

125 **Figure 1. Seasonal variations in the occurrence frequency of pure dust (left panels) and polluted dust (right panels) derived from CALIOP observations for 2007–2023. ERA5 850-hPa winds are overlaid as blue arrows. Black "+" symbols indicate grid cells where the target aerosol type accounts for more than 60 % of the total aerosol occurrences. Three hotspots are marked as white boxes in Figure 1e.**

https://doi.org/10.5194/egusphere-2026-4228
Preprint. Discussion started: 28 July 2026

3 Composition of polluted dust based on MERRA-2 reanalysis data

3.1 Modern-Era Retrospective analysis for Research and Applications, Version 2 (MERRA-2)

MERRA-2 provides species-resolved aerosol products that partition aerosol mass and aerosol optical depth (AOD) into dust, sea salt, sulfate, organic carbon, and black carbon components, allowing the climatological aerosol composition within polluted dust hotspots to be quantified. Since a significant fraction of polluted dust is likely to occur as internally mixed particles (i.e., dust cores coated by pollution aerosols), MERRA-2 is further used to characterize the coexisting aerosol species within the CALIOP-identified polluted dust hotspots and to provide reanalysis-based compositional context for subsequent mixing state experiments. In this study, monthly mean two-dimensional diagnostic products are used to examine the climatological seasonal cycles of aerosol loading, sources, and transport. Specifically, tavgM_2d_adg_Nx is used to analyze species-resolved aerosol emissions, while tavgM_2d_aer_Nx provides species-resolved column AOD at 550nm and aerosol mass horizontal flux.

For subsequent optical property calculations and DRE experiments, three-hourly three-dimensional aerosol mass mixing ratios from inst3_3d_aer_Nv are employed at a horizontal resolution of 0.625° in longitude by 0.5° in latitude, with a typical vertical resolution of about 15 hPa. The 3-hourly temporal resolution enables direct coupling with solar geometry (solar zenith angle), instantaneous atmospheric profiles, and the radiative transfer model, supporting time-consistent calculations of aerosol optical properties and radiative flux perturbations under different mixing state assumptions.

3.2 Climatological aerosol composition in polluted dust hotspots

Based on the 2007–2023 climatology, this context provides a baseline for interpreting the CALIOP-identified hotspots and helps inform the mixing state scenarios examined in subsequent sections. Figure 2 presents the monthly climatology of AOD for dust and major aerosol components (sulfate, organic carbon, black carbon, and sea salt) over the three polluted dust hotspots identified in Sect. 2.2: West Central Africa, the Indian Subcontinent, and the Capital Region of China. For each hotspot region, we average the MERRA-2 column AOD data (tavgM_2d_aer_Nx) over the boxed region and then compute the climatological monthly mean over 2007–2023; the error bars indicate the interannual standard deviation of monthly AOD. Across the three hotspots, dust AOD exhibits a pronounced seasonal cycle, while coexisting pollution aerosols—especially sulfate and organic carbon—display region-dependent seasonal variability.

https://doi.org/10.5194/egusphere-2026-4228
Preprint. Discussion started: 28 July 2026

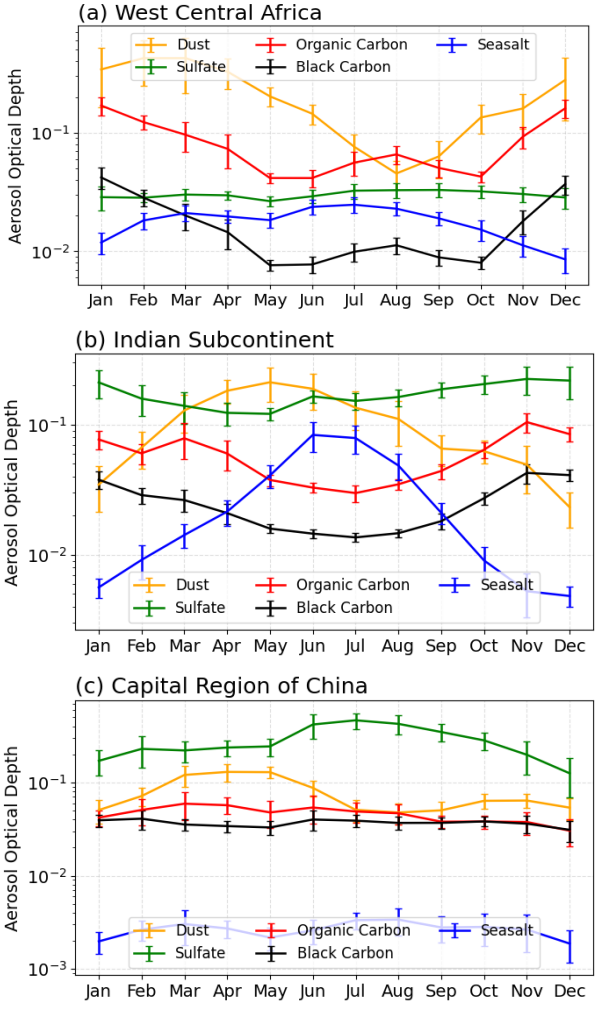

Figure 2. Monthly climatology (2007–2023) of aerosol optical depth (AOD) at 550nm for dust and major aerosol components (sulfate, organic carbon, black carbon, and sea salt) over three polluted dust hotspots, based on the MERRA-2 reanalysis. Panels (a)–(c) correspond to West Central Africa, the Indian Subcontinent, and the Capital Region of China, respectively. Error bars indicate the interannual standard deviation of monthly AOD over 2007–2023.

To further characterize the vertical distribution of pollutants and dust in each hotspot, we analyze the MERRA-2 aerosol mixing ratio reanalysis product (inst3_3d_aer_Nv) and examine the DJF climatological vertical profiles of dust and major coexisting pollutant species, including sulfate, organic carbon, black carbon, and sea salt (Fig. 2). These profiles reveal distinct pollutant–dust mixing regimes among the hotspots: organic carbon is the dominant pollutant mixed with dust by mass in west central Africa, sulfate dominates in the capital region of China, and over the Indian subcontinent the dominant pollutant varies with altitude, with organic carbon prevailing in elevated dust layers near 10 km and sulfate dominating lower dust layers around 2.5 km.

https://doi.org/10.5194/egusphere-2026-4228
Preprint. Discussion started: 28 July 2026

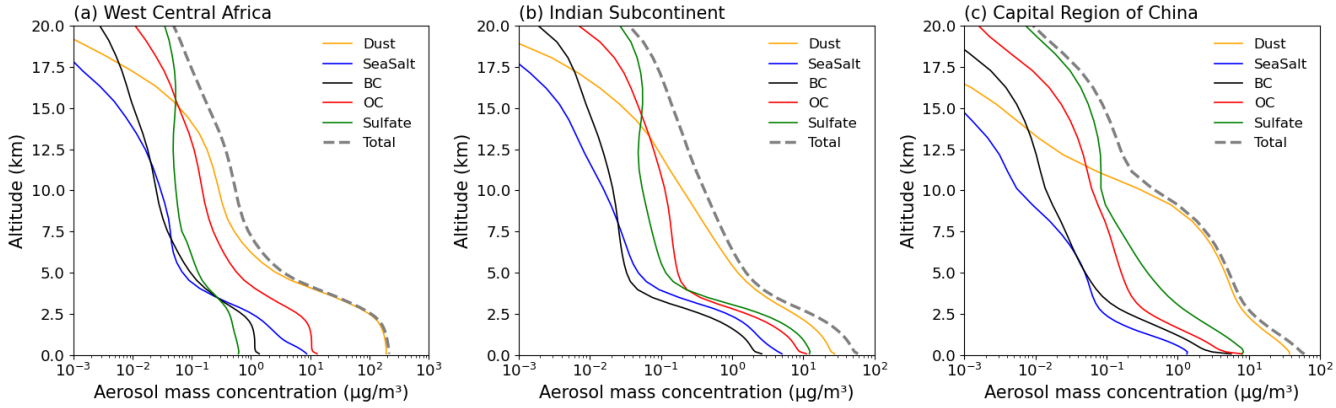

Figure 3. Climatological vertical profiles of aerosol mass concentration (μg/m³) in DJF, averaged over 2007–2023 from MERRA-2 inst3_3d_aer_Nv reanalysis, for three representative polluted dust hotspots: (a) West Central Africa (6–9°N, 15°W–0°), (b) the Indian Subcontinent (18–26°N, 70–85°E), and (c) the Capital Region of China (36–40°N, 110–117°E).

To place the MERRA-2 climatology in an observational context, we combine satellite AOD and occurrence statistics with the reanalysis fields (Fig. 4). The top row compares monthly mean total AOD and dust AOD from MERRA-2 and CALIOP, where the CALIOP dust AOD at 532nm is derived using the depolarization-based dust separation and AOD partition scheme of Song et al. (2021). The comparison indicates that the two datasets capture broadly consistent timing and phase of the dust-active seasons, although MERRA-2 generally underestimates dust AOD relative to the CALIOP-based estimates, especially during the peak-dust months. The green shading, which brackets the low and high CALIOP dust AOD estimates, indicates that the MERRA-2–CALIOP differences are comparable to the uncertainty range of the satellite retrievals.

The occurrence statistics in the bottom row of Fig. 4 provide additional context for interpreting the AOD climatology. In each hotspot, polluted dust occurrence frequency peaks during the dust-active seasons and remains low when dust DAOD is small, indicating that polluted dust tends to form when substantial dust plumes are present. The fraction of polluted dust relative to all aerosol layers and to all dusty aerosol layers (dust, polluted dust, and marine dust) also shows distinct regional behavior: West Central Africa is characterized by a large polluted dust fraction during boreal winter and spring, the Indian Subcontinent exhibits a sharp increase during the pre-monsoon seasons, and the Capital Region of China maintains high polluted dust fractions throughout much of the year. These patterns confirm that the three hotspots represent regimes where mineral dust and pollution aerosols frequently co-exist, and therefore provide suitable testbeds for assessing how pollutant mixtures modify dust optical properties and direct radiative effects in the following sections. Although MERRA-2 systematically underestimates DAOD relative to CALIOP, it captures a broadly consistent seasonal phase, supporting its use to identify dust-active periods and provide compositional context. This low bias may affect the absolute magnitude of the estimated radiative effects, but should have limited influence on the relative comparison among the prescribed aerosol mixing states.

https://doi.org/10.5194/egusphere-2026-4228
Preprint. Discussion started: 28 July 2026

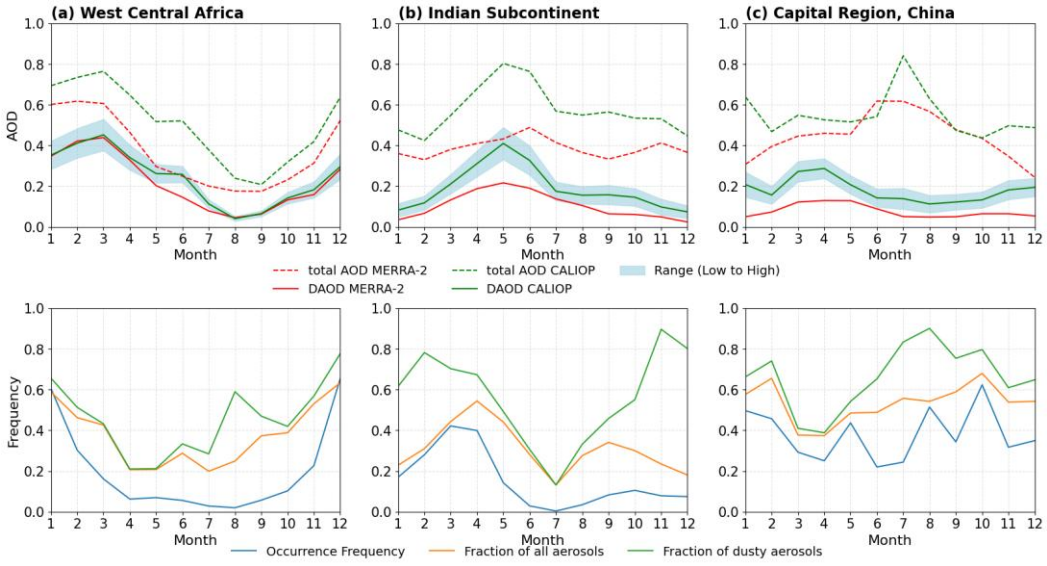

Figure 4. Seasonal cycle of dust and polluted dust over three hotspot regions, averaged over 2007–2023. Top row: monthly mean total AOD (dashed) and dust AOD (DAOD; solid) from MERRA-2 (red) and CALIOP (green). Blue shading denotes the range between the low and high dust AOD estimates derived from CALIOP. Bottom row: monthly occurrence statistics of CALIPSO polluted dust aerosol, including its occurrence frequency (blue), its fraction relative to all aerosol layers (orange), and its fraction relative to all dusty aerosol layers (dust + polluted dust + dusty marine; green). Panels (a)–(c) correspond to West Central Africa, the Indian Subcontinent, and the Capital Region of China, respectively.

To further investigate why polluted dust tends to occur in specific seasons and regions, we examine the spatial relationship between dust emission, mass flux, and co-located pollutant sources using the MERRA-2 Aerosol Diagnostics (extended) data set (tavgM_2d_adg_Nx; Fig. 5). Over West Central Africa in MAM, strong dust emission and column mass flux are concentrated along the southern edge of the Sahara, while the top 3 % organic carbon emissions are located mainly to the south over the tropical biomass burning belt. This configuration supports a source–receptor picture in which dust exported from the Sahara is advected southward and becomes mixed with locally emitted organic aerosols over the polluted dust hotspot identified by CALIOP.

In DJF over the Indian Subcontinent and eastern China, dust emission and transport maxima are situated to the west and northwest of the receptor regions, whereas the highest sulfate emissions are collocated with densely populated and industrialized areas within the hotspots. The dust mass-flux vectors indicate that dust plumes originating from upwind arid regions are transported across these pollution centers, providing ample opportunity for sulfate coatings to form on transported dust. Taken together, the patterns in Fig. 5 are consistent with the occurrence statistics in Fig. 1 and 4, and they reinforce the view that polluted dust in these three hotspots is generated primarily by the interaction between long-range transported dust and strong local pollution sources.

https://doi.org/10.5194/egusphere-2026-4228
Preprint. Discussion started: 28 July 2026

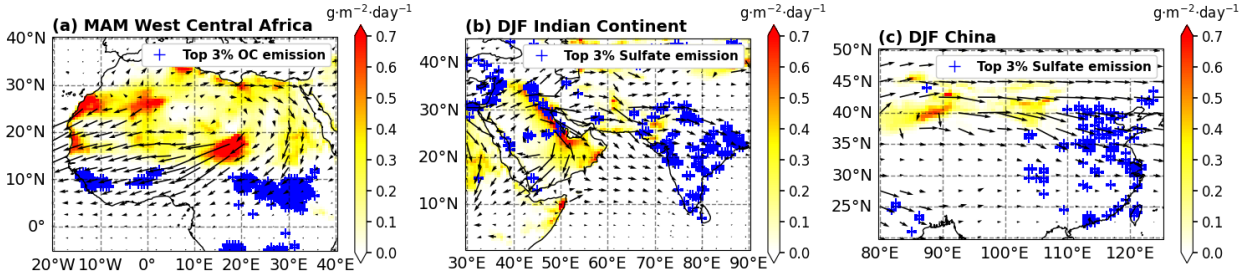

Figure 5. Local dust emission rate (shading) derived from the MERRA-2 Aerosol Diagnostics (extended) data set over three polluted dust hotspots. Blue "+" symbols indicate grid cells where local pollutant aerosol emission rates exceed the 97th percentile within each panel's domain (organic carbon in panel (a), sulfate in panels (b) and (c)). Dust column mass-flux vectors from the MERRA-2 Aerosol Diagnostics data set are overlaid as arrows.

4 Sensitivity of aerosol DRE to the mixing state of polluted dust in China

4.1 Schemes for dust mixing with pollution aerosols

Since a significant fraction of polluted dust is likely to consist of internally mixed particles—dust cores coated with pollution aerosols such as sulfate and nitrate, as suggested by in-situ and single-particle observations and by global model studies (Jordan et al., 2003; Krueger et al., 2004; Li and Shao, 2009; Bauer and Koch, 2005; Bauer et al., 2007; Tian et al., 2018)—we simulate the optical properties of internally mixed polluted dust and quantify the resulting radiative impacts in our idealized experiments. We first develop a simple theoretical mixing framework, following the approach of Zhang et al. (2024), and then use it to compute dust optical properties and direct radiative effects in both the shortwave and longwave spectrum.

Following previous studies, we represent internally mixed polluted dust as concentric spherical core–shell particles, with mineral dust as the core and pollution aerosols forming the shell (e.g., Bauer et al., 2007; Zhang et al., 2024; Figure 6). Although this geometry is idealized, microscopic observations show that core–shell–like particles occur in substantial numbers under a variety of regional and environmental conditions (Unga et al., 2018), suggesting that this simplified mixing model would be adequate for assessing the first-order impacts of surface coatings on dust DRE. We compare an externally mixed polluted dust population with three internal mixing schemes in which the pollutant aerosol mass is coated onto dust cores as shells, forming concentric core–shell particles. The dust and sulfate mass distributions are taken from the MERRA-2 aerosol mixing ratio reanalysis product (inst3_3d_aer_Nv), with dust represented by the five MERRA-2 dust size bins. In the externally mixed reference case, sulfate is represented as a separate aerosol population with a uniform dry effective radius of 0.35 μm, while the total dust and sulfate masses are kept identical to those in the internal mixing cases. The three internal-mixing schemes differ only in how the sulfate shell volume is distributed among dust size bins: in Scheme I, the shell volume allocated to each dust particle is proportional to its diameter; in Scheme II, it is proportional to the particle surface area; and in Scheme III, it is proportional to the particle volume. Consequently, Scheme I preferentially coats finer dust particles, Scheme III concentrates the coating on coarser particles, and Scheme II represents an intermediate case. These schemes are designed to bracket uncertainties associated with different physical coating mechanisms and to test how the size-dependent placement of sulfate

https://doi.org/10.5194/egusphere-2026-4228
Preprint. Discussion started: 28 July 2026

coatings affects polluted dust optical properties and DRE. For each coated size bin, optical properties are calculated using the concentric core–shell Mie code implemented in PyMieScatt (Sumlin et al., 2018).

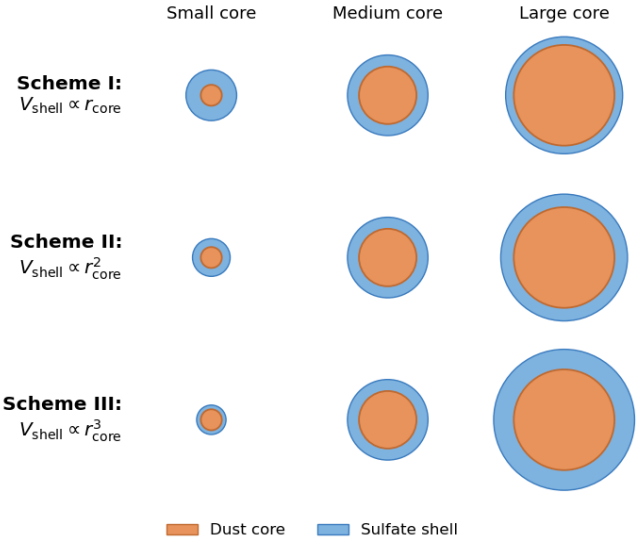

Figure 6. Schematic illustration of the three idealized dust–sulfate internal mixing schemes used in this study. Dust cores are shown in orange and sulfate shells in blue. From left to right, the sulfate shell volume assigned to each particle is proportional to dust-core diameter (Scheme I), surface area (Scheme II), and volume (Scheme III), while the total masses of dust and sulfate are conserved across schemes.

The optical properties derived for each mixing state are then combined with the MERRA-2 dust and sulfate fields to quantify AOD at 550 nm and 10 μm, representing shortwave and longwave extinction, respectively. To provide a concrete regional example in which internal mixing effects are expected to be most apparent, the following analysis focuses on May 2010 over the eastern China coastal region (110–125°E, 35–45°N), including the Capital Region of China polluted dust hotspot identified in Sect. 2.2. This month is selected because the time series indicates a sulfate-rich background coincident with substantial dust loading, thereby amplifying the sensitivity of AOD and radiative effects to the assumed internal mixing scheme. Figure 7 illustrates how the assumed dust–sulfate mixing state can substantially modulate regional AOD in a polluted dust regime. At 550 nm, dust AOD over the eastern China coastal region in May 2010 is moderate and slightly lower than sulfate AOD, but the two are of comparable magnitude (panels a–b), with sulfate exhibiting a distinct spatial maximum. Treating dust and sulfate as a fully external mixture yields a much larger total AOD field (panel c), reflecting the additive contribution from the sulfate component. In contrast, when sulfate is incorporated through internal mixing schemes I–III (panels d–f), the resulting polluted dust AOD remains closer to the pure dust baseline but is consistently enhanced, with relative increases of about 10–30% depending on the scheme and location (panels g–i). The enhancement is largest where sulfate AOD is highest (i.e., within and around the Capital Region hotspot), indicating that the 550 nm AOD response to internal mixing is primarily controlled by the local sulfate burden available for coating. Relative to the fully external mixture reference, however, the contour lines show

https://doi.org/10.5194/egusphere-2026-4228
Preprint. Discussion started: 28 July 2026

that fully internal mixing can reduce AOD at 550 nm by up to 60% over parts of the domain. The strongest reductions occur in and around the sulfate-rich hotspot.

At 10 μm (Figure 8), pure sulfate contributes little to the external-mixture AOD (panel b), so the fully external mixture AOD largely resembles the dust spatial pattern (panel c). However, internal mixing produces a markedly larger fractional perturbation than at 550 nm. Schemes I–III yield widespread AOD increases of ~20–50% relative to pure dust and ~5–15% relative to the fully external-mixture reference (panels g–i), with the largest enhancements concentrated over the sulfate-rich part of the domain. This enhanced sensitivity at 10 μm suggests that internal mixing can exert a larger influence on longwave extinction—and hence longwave DRE—than would be inferred from shortwave diagnostics alone. This point is particularly relevant because many models still assume externally mixed optics for polluted dust, while the longwave radiative impacts remain less well constrained.

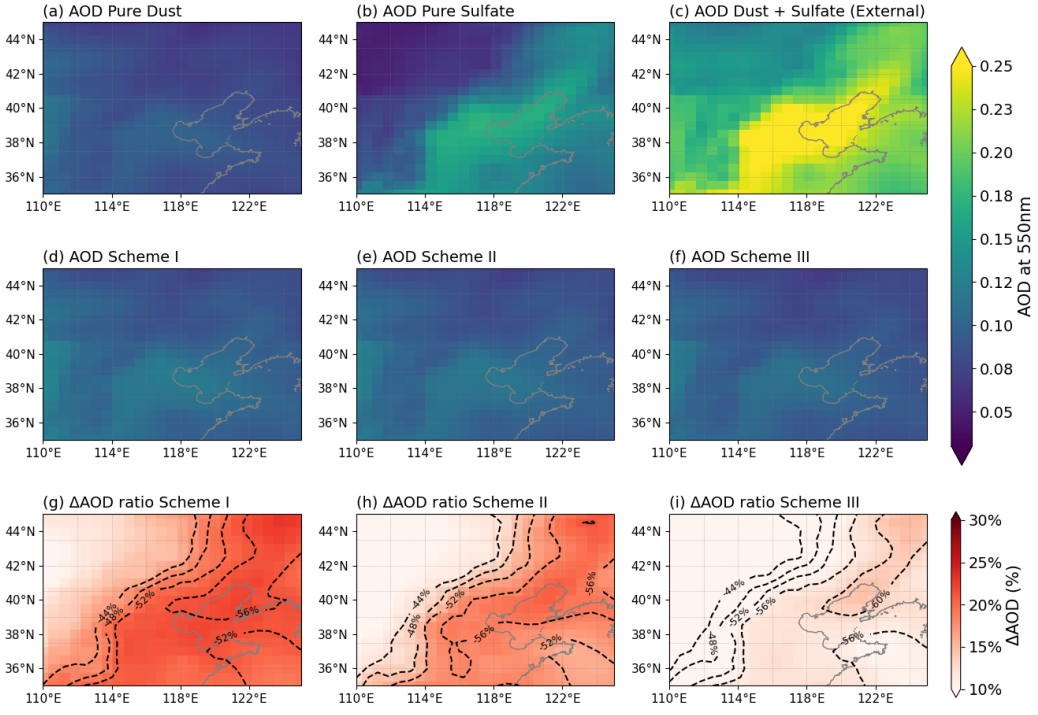

Figure 7. Changes in 550 nm dust aerosol optical depth (AOD) associated with internal mixing with sulfate over the Capital Region of China in May 2010. Panels (a) and (b) show baseline AOD for pure dust and pure sulfate, respectively. Panel (c) shows the AOD for dust + sulfate treated as an external mixture. Panels (d)–(f) show polluted dust AOD after mixing with sulfate using internal mixing schemes I–III. Color shading in panels (g)-(i) shows the relative AOD change with respect to pure dust, calculated as ($AOD_{internal}$ - AOD_{pure}) / AOD_{pure} × 100%. The dashed contours in panel (g)-(i) show the relative difference between each internal mixing scheme and the externally mixed case, calculated as ($AOD_{internal}$ − $AOD_{external}$) / $AOD_{external}$ ×100%.

https://doi.org/10.5194/egusphere-2026-4228
Preprint. Discussion started: 28 July 2026

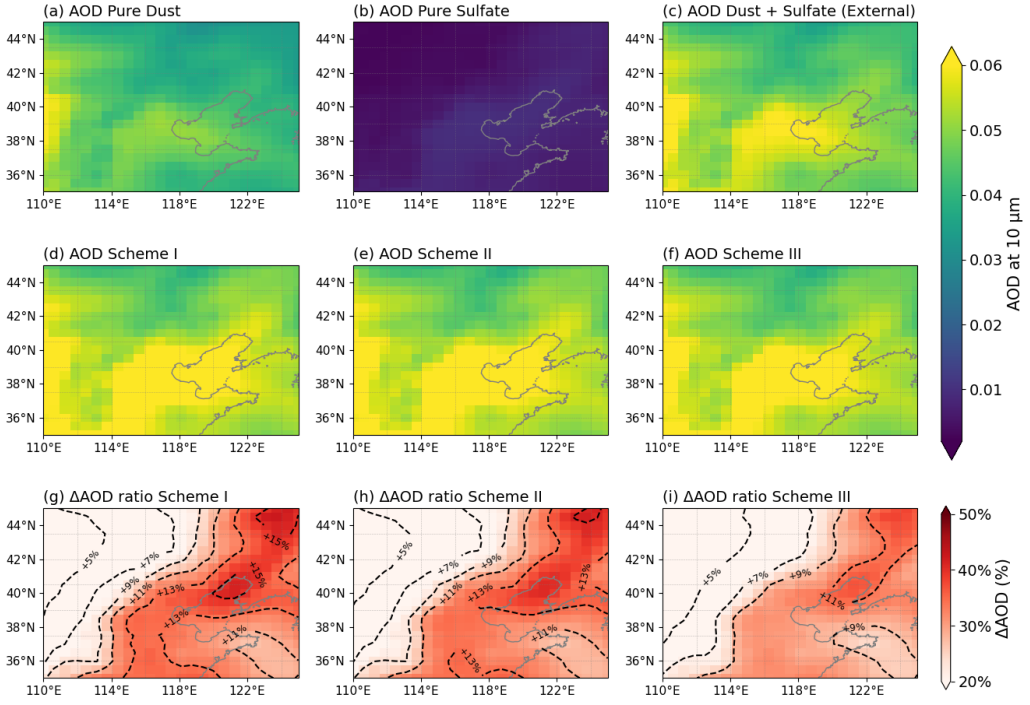

Figure 8. Same as Figure 7, but for dust aerosol optical depth (AOD) at 10 μm.

The domain averaged vertical structure at 550 nm reflects the different preferred altitudes of dust and sulfate over the Capital Region of China in May 2010 (Figure 9). The extinction coefficients of both pure dust and pure sulfate are largest in the lower troposphere and generally decrease with altitude, with sulfate more strongly confined below about 4 km. Adding sulfate as an externally mixed component therefore produces the largest enhancement in low-level extinction. In contrast, the three internal mixing schemes redistribute the sulfate mass onto the dust cores and primarily enhance extinction within the existing dust layers. As a result, the internally mixed profiles thus closely follow the shape of the pure dust profile and generally fall between the pure dust and full externally mixed dust curves in magnitude.

At 10 μm, the enhancement of the extinction profiles due to sulfate is much weaker than at 550 nm. Compared with pure dust, both external and internal mixing enhance LW extinction throughout the dust layer, with the internally mixed cases producing larger increases than the externally mixed case. The three internal mixing schemes yield profiles that are very similar to one another, indicating that the detailed size dependence of the coating has little impact on LW extinction. In particular, for a given sulfate burden, the vertically integrated 10 μm extinction AOD is systematically higher in the internal mixing cases than in the external mixing case, while differences among the assumed internal mixing states only exert a secondary influence. An interesting contrast between 550nm and 10μm is that, at 550nm the AOD of internal mixture is smaller than the full external mixing. But at 10μm, the internal mixture has a larger AOD than external mixture. This wavelength dependence is consistent with Zhang et al. (2024) and reflects the different extinction behavior of sulfate and dust across the spectrum. At 550 nm, externally mixed sulfate contributes a large number of small particles with a large total geometric cross section, leading to stronger extinction. At 10 μm, however, sulfate has a much lower extinction efficiency than dust. When sulfate is coated on dust particles, the coated particles retain relatively high longwave extinction efficiency, making internal mixing more effective than external mixing in increasing 10 μm AOD.

https://doi.org/10.5194/egusphere-2026-4228
Preprint. Discussion started: 28 July 2026

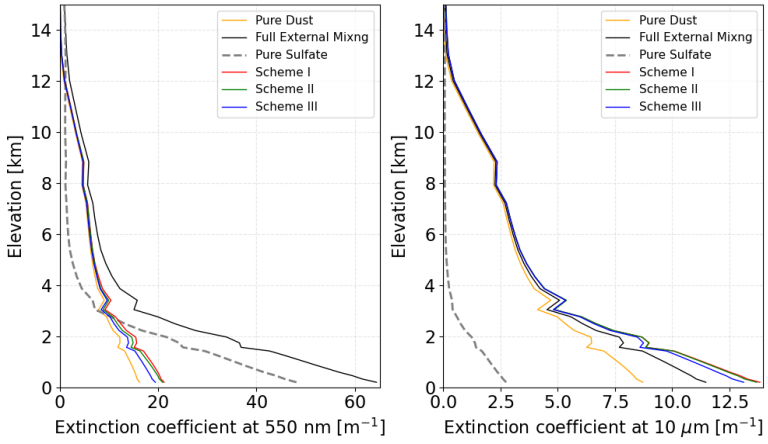

Figure 9. Vertical profiles of bulk aerosol extinction coefficient (m^{-1}) at (a) 550 nm and (b) 10 μm for different dust–sulfate mixing states, averaged over the Capital Region of China in May 2010. Colored solid lines show pure dust (orange), fully externally mixed dust–sulfate (black), and internally mixed schemes I–III (red, green, and blue), while the gray dashed line denotes pure sulfate.

To establish the microphysical basis for the subsequent radiative effect analysis, the bulk optical properties of the dust-sulfate mixture are diagnosed. Building on the mixing framework described in Section 4.1, size-resolved extinction efficiency ⟨Q_e⟩, single-scattering albedo ⟨ω⟩, and asymmetry factor ⟨g⟩ are calculated for each dust size bin and mixing state. For each sulfate mixing state, the internally mixed sulfate fraction is prescribed as $f_{internal}$ = 0%, 25%, 50%, 75% or 100%, with the coating mass distributed among dust size bins according to one of the three core–shell schemes. When $f_{internal}$ < 100%, the remaining sulfate mass is treated as externally mixed homogeneous spheres, and its optical properties are computed with the same Mie solver. For each wavelength and mixing state, the size-resolved optical properties are combined with the vertical profiles of size-resolved mass: for each size bin, extinction and associated ω and g are first vertically integrated, and the angle brackets in Figure 10 denote column bulk averages across all the size bins, weighted by their column extinction, yielding ⟨Q_e⟩, ⟨ω⟩, and ⟨g⟩ for the dust–sulfate mixture.

As the internal sulfate fraction increases from 25 % to 100 % (Fig. 10), the bulk shortwave optics at 550 nm (solid lines in Fig. 10a–c) change systematically. ⟨Q_e⟩ and ⟨ω⟩ both decrease as more sulfate is moved from the external mixture onto dust cores, indicating weaker shortwave scattering and slightly stronger absorption for the polluted dust ensemble. In contrast, ⟨g⟩ shows a weakly non-monotonic response: in Schemes I and II, a modest maximum appears at intermediate internal fractions (about 25–75 %), and all three schemes converge to slightly lower ⟨g⟩ at 100 % internal mixing than in the predominantly external-mixing case. The overall sensitivity still depends on the coating pattern, with Scheme III producing the largest net decrease in ⟨Q_e⟩ and ⟨ω⟩, Scheme I the smallest, and Scheme II in between. At 10 μm, the impact of sulfate on the bulk optical properties is weaker than at 550 nm. Increasing the internal sulfate fraction leads to modest increases in ⟨Q_e⟩ and ⟨ω⟩ for all three schemes (dashed lines in Fig. 10a–b), with Scheme III showing the largest enhancement and Scheme I the smallest, and Scheme II

https://doi.org/10.5194/egusphere-2026-4228
Preprint. Discussion started: 28 July 2026

falling in between. The response of ⟨g⟩ is more scheme dependent: in Schemes I and II, ⟨g⟩ decreases as the internal fraction increases, whereas in Scheme III it increases slightly (dashed lines in Fig. 10c).

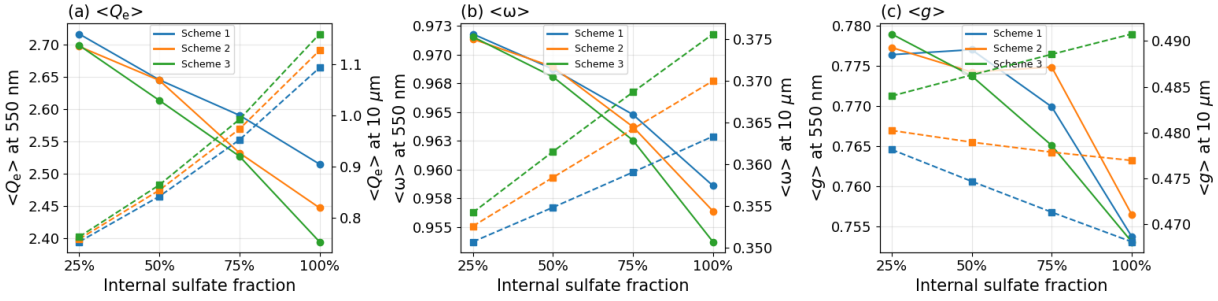

Figure 10. Bulk averaged extinction efficiency ⟨Q_e⟩ (panel a), single-scattering albedo ⟨ω⟩ (panel b), and asymmetry factor ⟨g⟩ (panel c) as a function of internal sulfate fraction for mixing schemes I–III. Solid lines denote values at 550 nm, and dashed lines denote values at 10 μm.

4.2 Impacts of mixing state on dust DRE

To assess how the dust–sulfate mixing state modifies dust radiative effects over the eastern China coastal region, radiative fluxes are computed using the Rapid Radiative Transfer Model (RRTM), using RRTM_SW for the shortwave spectral range of 0.2–12.2 μm and RRTM_LW for the longwave spectral range of 3.08 – 1000 μm, under both aerosol-loaded and aerosol-free (pristine) atmospheric conditions. The resulting vertically resolved extinction, single-scattering albedo, and asymmetry factor in each RRTM band are then combined with standard atmospheric profiles and applied over the eastern China coastal region (110°E–125°E, 35°N–45°N). The shortwave surface albedo is taken from the MERRA-2 tavg1_2d_rad_Nx radiation diagnostics product, and the longwave surface emissivity is taken from a satellite-based emissivity dataset (Huang et al., 2016). We diagnose shortwave and longwave dust direct radiative effects at the top of the atmosphere (TOA) and at the surface as the difference in net flux between dusty and clean atmospheres at each grid cell, and then compute domain averages over land and ocean separately. Figure 11 summarizes the resulting land-mean and ocean-mean DRE as a function of the fraction of sulfate internally mixed with dust, with the pure dust DRE indicated by horizontal purple lines.

In the shortwave, dust exerts a negative DRE (cooling) at both TOA and the surface. As the internal sulfate fraction increases from 0 % (all sulfate externally mixed) to 100 %, the SW DRE becomes progressively less negative for all three schemes, over both land and ocean. This weakening of the cooling effect is consistent with the reduction in bulk ⟨Q_e⟩ and total extinction cross-section at 550 nm when sulfate is transferred from the external mixture onto dust cores (Fig. 10a). The sensitivity is more pronounced over ocean than over land because the dark ocean surface has a lower albedo, so changes in dust scattering more effectively modify the planetary reflectance. For a fixed internal fraction, differences among schemes are most evident in the SW: Scheme I, which concentrates coatings on fine dust, maintains the largest (most negative) SW cooling, whereas Scheme III, which coats coarse dust, yields the weakest cooling, with Scheme II in between. In the longwave, dust produces a positive

https://doi.org/10.5194/egusphere-2026-4228
Preprint. Discussion started: 28 July 2026

DRE (warming) by trapping outgoing terrestrial radiation. Increasing the internal sulfate fraction enhances the LW DRE at both TOA and the surface, but the magnitude of this enhancement is much smaller than the SW change. This LW enhancement occurs because sulfate coatings increase the outer radius of dust particles, pushing part of the dust–sulfate population closer to the longwave size-parameter regime where extinction is more efficient. As a result, internal mixing slightly enhances longwave warming relative to external mixing, even though the total column extinction cross section is reduced. The positive LW DRE is systematically larger over land than over ocean, reflecting the higher surface longwave emissivity of land relative to the adjacent sea. At a given internal fraction, differences among Schemes I–III in LW DRE are modest compared with those in the SW, consistent with the weaker dependence of longwave bulk optics on the detailed size distribution of the sulfate coating. Treating polluted dust as fully externally mixed substantially overestimates its net cooling effect relative to the fully internally mixed cases. In the net DRE panels (Fig. 11c, f), Averaged over the three internal schemes, the net DRE changes from −4.94 to −2.55 W m^{-2} at the TOA and from −6.19 to −3.83 W m^{-2} at the surface over land, corresponding to cooling reductions of 48.4% and 38.1%, respectively. Over ocean, the net DRE changes from −8.70 to −5.01 W m^{-2} at the TOA and from −9.36 to −5.61 W m^{-2} at the surface, corresponding to reductions of 42.4% and 40.1%.

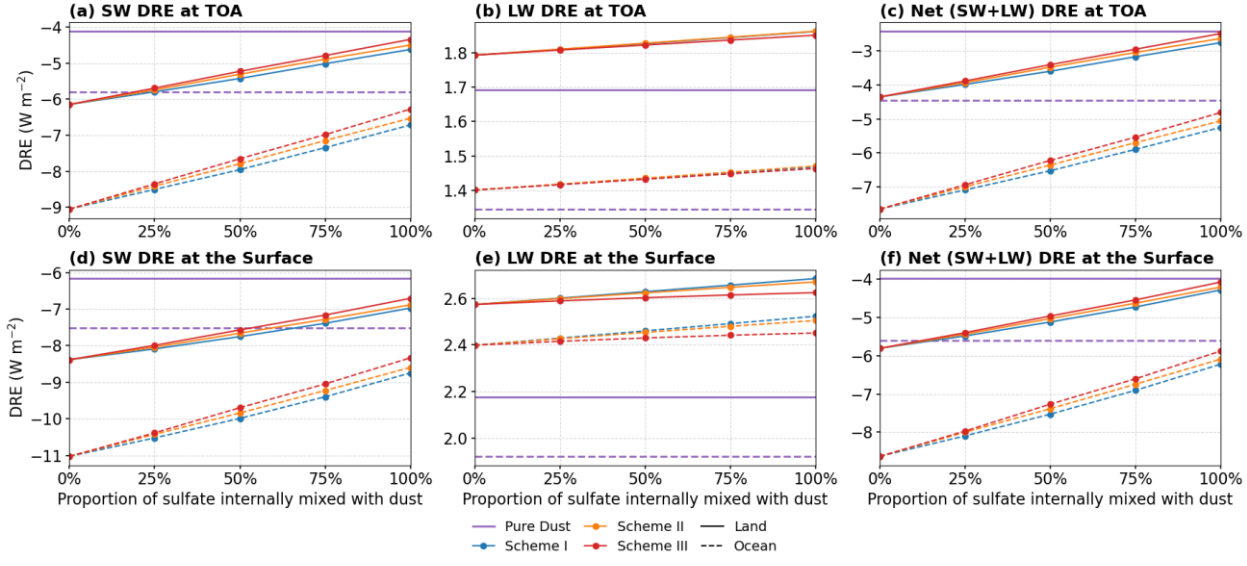

Figure 11. Dust direct radiative effect (DRE) as a function of the fraction of sulfate internally mixed with dust for mixing schemes I–III. The top row shows DRE at the top of the atmosphere (TOA), and the bottom row shows DRE at the surface. The left, middle, and right columns show shortwave (SW), longwave (LW), and net (SW + LW) DRE, respectively. Solid lines denote values over land, and dashed lines denote values over ocean. Horizontal purple lines indicate the corresponding DRE of pure dust.

The spatial expression of the SW mixing state effect over the eastern China coastal region in May 2010 is shown in Figs. S6 and S7 for the TOA and surface, respectively. In each figure, panels (a) and (e) show the reference DRE fields for pure dust and fully externally mixed polluted dust, while panels (b)–(d) show the DRE differences between internally mixed Schemes I–III and pure dust, and panels (f)–(h) show the corresponding differences relative to the fully external mixture. At both the TOA and surface, the fully externally mixed case produces the strongest SW cooling, with large negative DRE values over the

https://doi.org/10.5194/egusphere-2026-4228
Preprint. Discussion started: 28 July 2026

Capital Region of China hotspot identified in Sect. 2.2 and the adjacent seas, broadly collocated with enhanced sulfate loading. The internally mixed cases are also more negative than pure dust, indicating that the addition of sulfate enhances SW cooling relative to pure dust. However, their differences relative to the external mixture are mostly positive, demonstrating that internal coating substantially weakens the sulfate-induced enhancement of SW cooling compared with an external mixture. Notably, the DRE difference between the external and internal mixtures is several times larger than that between pure dust and the internal mixtures, underscoring the strong sensitivity of the sulfate DRE contribution to the assumed mixing state. This contrast reflects the stronger scattering contribution of externally mixed sulfate particles relative to sulfate redistributed as coatings on dust cores. This interpretation is further supported by the SW flux-component diagnostics. The externally mixed case produces the largest increase in aerosol-induced upward SW flux at the TOA, with the regional mean increasing from approximately 4.4 W m^{-2} for pure dust to 7.4 W m^{-2}, compared with about 5.0 W m^{-2} for the internally mixed schemes (Fig. S12). The corresponding surface response shows reduced downwelling SW flux for all aerosol cases, again with the strongest reduction in the fully external mixture (Fig. S13). Thus, the similar TOA and surface DRE patterns reflect enhanced solar reflection at the TOA and reduced solar transmission to the surface. The weaker, smoother responses of Schemes I–III are consistent with the smaller SW extinction enhancement of coated dust relative to externally mixed sulfate.

In contrast, adding sulfate has only a limited impact on the LW DRE relative to pure dust (Figs. S8 and S9). Differences relative to pure dust are generally substantially smaller in magnitude than the corresponding SW differences. The internally mixed schemes produce slightly stronger LW warming than the fully external mixture (panels f-h in Figs. S8 and S9) and scheme I has the strongest warming enhancement, consistent with the increase in LW AOD when sulfate is incorporated as coatings on dust cores (Fig. 8). At TOA, this enhancement is more evident over land, where stronger surface thermal emission provides more upward LW radiation for absorption by the polluted dust layer (Fig. S8). At the surface, the response is spatially similar but shows a weaker land–sea contrast, suggesting that surface LW DRE differences are controlled primarily by absorption and re-emission within the aerosol layer rather than by surface properties alone (Fig. S9). The LW flux diagnostics further support this interpretation: all dusty cases reduce the upward LW flux at the TOA by approximately 1.6–1.9 W m^{-2} relative to clean sky, with slightly larger reductions for internally mixed particles (Fig. S14), while all dusty cases increase the downward LW flux at the surface, again with modestly larger values for the internally mixed cases (Fig. S15). Thus, sulfate coatings modestly enhance LW trapping, but the weak sensitivity among mixing states indicates that the overall mixing-state dependence of dust DRE is dominated by SW flux changes.

The atmospheric DRE, defined as TOA minus the surface DRE, represents the radiative energy deposited in the atmospheric column induced by aerosols. Figures S10 and S11 show the atmospheric DRE of pure dust and polluted dust in SW and LW, respectively. In the SW (Fig. S10), the differences between the internally mixed schemes and pure dust are generally positive, indicating that the addition of sulfate increases atmospheric SW absorption rather than producing a purely scattering perturbation. The atmospheric DRE difference (internal minus external; panels f–h) reverses sign with sulfate loading, being negative over the sulfate-rich region and weakly positive elsewhere. This pattern suggests that, where sulfate abundance is

https://doi.org/10.5194/egusphere-2026-4228
Preprint. Discussion started: 28 July 2026

high, externally mixed sulfate enhances multiple scattering and increases the probability of absorption by dust, leading to larger column absorption than in internally mixed cases. Where sulfate AOD is low, the weakly positive differences between internal and external mixing are consistent with a coating induced lensing effect, in which the sulfate shell enhances the absorption efficiency of the dust core. In the LW (Fig. S11), both internal and external dust–sulfate mixtures produce more negative atmospheric DRE than pure dust, reflecting enhanced LW emission and absorption by polluted dust layers. The internally mixed cases generally show more negative atmospheric DRE than the external mixture, with Scheme III being the only exception (panels f-h). This exception arises from the balance between enhanced LW extinction and changes in single-scattering albedo. In Scheme III, the relatively high LW single-scattering albedo shown in Fig. 10 partly offsets the emissivity increase associated with enhanced LW extinction, thereby weakening the atmospheric DRE response.

To synthesize the spatial analyses above, Figure 12 summarizes the regional-mean SW and LW DREs over the Capital Region of China hotspot (36–40°N, 110–117°E) for pure dust, the fully externally mixed case, and the fully internally mixed cases. In the SW, the externally mixed case produces by far the strongest cooling at both the TOA (−7.83 W m^{-2}) and the surface (−10.45 W m^{-2}), substantially exceeding pure dust (−4.83 and −7.12 W m^{-2}), whereas the internal mixture lies in between (−5.30 and −7.98 W m^{-2}). It is worth noting that the SW atmospheric DRE of the internal mixture (+2.68 W m^{-2}) is the strongest one among the three, because of the lensing effect explained in Zhang et al. (2024). The magnitude of the LW response is smaller than that of the SW response and has the opposite sign, but it reinforces the external–internal contrast in net DRE. Internal mixing produces stronger LW warming than both pure dust and the external mixture at both the TOA and the surface, contesting an enhanced LW absorption and emission by sulfate-coated dust cores. Relative to the external mixture, the internally mixed case reduces net cooling by 2.65 W m^{-2} at the TOA and 2.64 W m^{-2} at the surface, corresponding to 46.4% and 38.0% of the magnitude of the external-mixture net DRE, respectively.

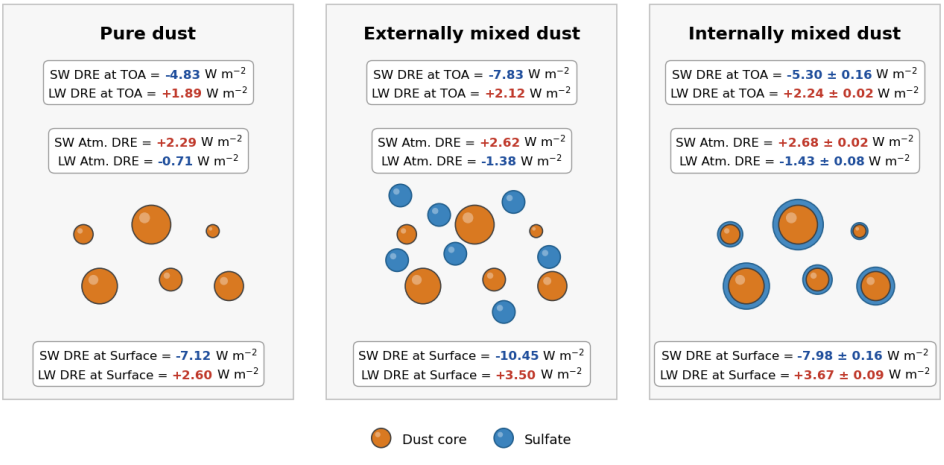

Figure 12. Conceptual diagram of the three dust–sulfate mixing states in this study: pure dust, externally mixed dust and sulfate, and internally mixed dust–sulfate particles. Orange and blue spheres denote dust cores and sulfate, respectively. The text boxes summarize the corresponding SW and LW DREs at the TOA, within the atmosphere, and at the surface, where the atmospheric

https://doi.org/10.5194/egusphere-2026-4228
Preprint. Discussion started: 28 July 2026

DRE is defined as the TOA DRE minus the surface DRE. Values are spatial means over the Capital Region of China (36–40°N, 110–117°E); for the internally mixed case, values are reported as the mean ± one-half of the range across Schemes I–III under fully internal sulfate mixing.

5 Discussions and Conclusions

The interaction between long-range transported mineral dust and co-located pollution, such as sulfate, nitrate, organic carbon, and soot from biomass burning or combustion sources, can generate polluted dust across a continuum of mixing states. These include external mixtures of dust and pollutant particles, core–shell dust particles with soluble coatings, and internally mixed dust–soot aggregates. Representing this diversity in mixing state is essential because each configuration can modify aerosol extinction, absorption, scattering directionality, and ultimately the shortwave and longwave direct radiative effects of dust. Previous work has emphasized shortwave consequences of dust aging, whereas corresponding impacts on longwave extinction and LW DRE—and the physical drivers of those responses—remain comparatively less constrained. This study addresses that gap by (i) using CALIOP (2007-2023) to identify recurring polluted dust hotspots, (ii) characterizing coexisting aerosol composition with MERRA-2 (2007–2023), and (iii) quantifying SW/LW optical and radiative sensitivities using an idealized concentric core–shell representation with three coating schemes (I–III) and a fully externally mixed reference, coupled to RRTM_SW and RRTM_LW. The major findings are:

1. **Robust polluted dust hotspots and transport context.** CALIOP occurrence statistics identify three climatological polluted dust hotspots—West Central Africa, the Indian Subcontinent, and the Capital Region of China—where polluted dust exhibits both high occurrence frequency and large fractions relative to total aerosol-type occurrences in the corresponding seasons. The hotspot seasonality is consistent with source-to-receptor pathways inferred from ERA5 850-hPa winds and MERRA-2 dust column mass flux, supporting a framework in which dust exported from upwind desert regions frequently overlaps with strong local pollution sources in the downwind regions.
2. **Climatological aerosol composition in polluted dust hotspots.** MERRA-2 climatology over 2007–2023 indicates that dust loading in all three hotspots exhibits a pronounced seasonal cycle, while coexisting pollutant components show region-specific behavior. West Central Africa is characterized by strong co-occurrence of dust and organic carbon during boreal winter–spring, consistent with biomass burning influence, whereas the Indian Subcontinent and the Capital Region of China show substantial sulfate burdens during the dust-active months, reflecting dominant anthropogenic sources. Interannual variability of monthly AOD is comparatively small relative to the seasonal cycle, supporting the use of climatological seasonal diagnostics and motivating the hotspot-focused sensitivity experiments.
3. **Contrasting SW vs LW controls on AOD response to mixing state.** At 550 nm, the externally mixed dust–sulfate case produces the largest AOD enhancement, whereas internally mixed cases yield smaller increases, with scheme-dependent ordering consistent with coatings distributed preferentially onto fine (Scheme I) versus coarse dust (Scheme III). At 10 μm, the ordering reverses: internally mixed polluted dust produces larger fractional AOD enhancements than the externally mixed case, while differences among Schemes I–III are secondary. This wavelength

https://doi.org/10.5194/egusphere-2026-4228
Preprint. Discussion started: 28 July 2026

dependence reflects different dominant controls: SW AOD sensitivity is governed primarily by changes in the total (column) extinction cross section associated with adding an externally mixed sulfate component, whereas LW AOD sensitivity is governed primarily by changes in effective extinction efficiency ($\langle Q_e \rangle$) of the mixed dust–sulfate mixture.

4. **Dependence of SW and LW DRE on mixing state.** Over the eastern China coastal domain (110–125°E, 35–45°N), the dust–sulfate mixing state strongly modulates dust direct radiative effects. As the fraction of sulfate internally mixed with dust increases, the shortwave DRE becomes systematically less negative, while the longwave warming is modestly enhanced; the shortwave response is stronger over ocean than over land. The May 2010 spatial DRE difference patterns further show that the fully externally mixed case produces the strongest sulfate-related SW cooling over the Capital Region of China hotspot and adjacent seas, whereas the internally mixed schemes substantially reduce this perturbation. In the longwave, internal mixing slightly enhances dust warming relative to external mixing because sulfate coatings increase the effective longwave extinction of dust-containing particles. However, this enhancement is much smaller than the shortwave change, and the differences among the three internal mixing schemes are modest. The associated flux perturbations confirm that the dependence of net DRE on mixing state is controlled primarily by shortwave flux changes, while longwave effects provide a weaker compensating contribution. Quantitatively, treating polluted dust as fully externally mixed substantially overestimates the magnitude of net cooling relative to the fully internally mixed cases. Averaged across Schemes I–III, the net cooling is reduced by 48.4% at the TOA and 38.1% at the surface over land, and by 42.4% at the TOA and 40.1% at the surface over ocean. The Capital Region hotspot mean shows the same tendency: relative to the fully external mixture, internal mixing produces a less negative net DRE, corresponding to a relative warming effect that offsets 46.4% of the external-mixture net cooling at the TOA and 38.0% at the surface. Our results can be compared with the earlier assessment of Bauer et al. (2007), who examined sulfate and nitrate coatings on mineral dust using a concentric core-shell representation similar to that adopted here. They found that coatings alter the single-scattering properties of dust appreciably only when the shell exceeds roughly 20% of the core radius, and concluded that coated dust can therefore be approximated as pure dust in radiative calculations, without explicit treatment of the internal mixture. Our shortwave results largely support this approximation: at 550 nm, the differences between the internally mixed schemes and pure dust optics are secondary, and the shortwave sensitivity to mixing state is governed primarily by whether the sulfate mass contributes additional externally mixed extinction, rather than by coating-induced changes in the optical properties of the dust particles themselves. In the longwave, however, our results reveal a subtlety not captured by this approximation. Sulfate coatings increase the effective longwave extinction efficiency of dust-containing particles, so that internally mixed polluted dust produces a larger fractional AOD enhancement at 10 μm, and correspondingly a stronger longwave warming, than either pure dust or the equivalent externally mixed dust-sulfate combination. In other words, the "coated dust behaving as pure dust" approximation, albeit adequate in the shortwave, breaks down in the longwave,

https://doi.org/10.5194/egusphere-2026-4228
Preprint. Discussion started: 28 July 2026

where the internal mixture is the most efficient warming configuration. Because the LW DRE of dust partially offsets its SW cooling, neglecting this coating enhancement biases the net DRE of polluted dust toward stronger cooling in heavily polluted downwind regions. This SW-LW asymmetry in terms of the impacts of internal mixing on dust DRE is, to our knowledge, a new result of the present study.

Taken together, these results indicate that representing polluted dust as fully externally mixed can lead to a substantial overestimate of SW cooling and a smaller underestimate of LW warming relative to internally mixed, coated dust. When SW and LW effects are considered jointly, the external-mixing assumption yields a net DRE that is systematically more negative (cooling) than internally mixed cases.

Although the present analysis is idealized (core–shell spheres, prescribed coating allocations), it highlights physically interpretable pathways through which internal mixing alters dust radiative impacts and motivates the need for observational and modelling constraints on LW optics of polluted dust. Extending this framework to additional pollutant species (e.g., nitrate and absorbing carbonaceous coatings), incorporating nonsphericity and realistic mixing morphology, and evaluating against satellite and in situ constraints in polluted dust hotspots represent natural next steps for reducing uncertainty in dust radiative forcing.

Code and data availability

The dust and polluted dust layers analyzed in this study were identified using the CALIOP Level 2 5 km Merged Layer product, Version 4-51, which is available from the NASA Langley Atmospheric Science Data Center Distributed Active Archive Center under https://doi.org/10.5067/CALIOP/CALIPSO/CAL_LID_L2_05kmMLay-Standard-V4-51. The global dust aerosol optical depth and dust vertical extinction coefficient climatology derived from CALIOP were obtained from the dataset provided by Song et al. (2021), available at https://drive.google.com/drive/folders/1aQVupe7govPwR6qmsqUbR4fJQsp1DBCX?usp=sharing. The ERA5 monthly averaged pressure-level wind fields used in this study were obtained from the Copernicus Climate Data Store ERA5 monthly averaged data on pressure levels product, available under https://doi.org/10.24381/cds.6860a573. The MERRA-2 reanalysis products used for aerosol, meteorological, radiative, and surface fields are publicly available from the NASA Goddard Earth Sciences Data and Information Services Center, including the collections with DOIs https://doi.org/10.5067/LTVB4GPCOTK2, https://doi.org/10.5067/WWQSXQ8IVFW8, https://doi.org/10.5067/Q9QMY5PBNV1T, https://doi.org/10.5067/KLICLTZ8EM9D, and https://doi.org/10.5067/ME5QX6Q5IGGU. The global band-by-band surface emissivity data used to prescribe surface

https://doi.org/10.5194/egusphere-2026-4228
Preprint. Discussion started: 28 July 2026

emissivity in RRTM_LW were obtained from the dataset described by Huang et al. (2016), available at https://huang.engin.umich.edu/182-2/.

Author contributions

RW performed the analysis and prepared the manuscript; ZZ designed and supervised the study and secured funding support; JZ, QS, and HY contributed to the methodology and interpretation; all authors reviewed and edited the manuscript.

Competing interests

At least one of the (co-)authors is a member of the editorial board of Atmospheric Chemistry and Physics.

Acknowledgements

We acknowledge the use of AI tools, including OpenAI's ChatGPT (https://openai.com) and Anthropic's Claude (https://www.anthropic.com), during the revision of this manuscript. These tools were used to improve the readability and language of the text, refine paragraph structure, and correct grammatical phrasing. All final content, scientific arguments, and conclusions remain the sole responsibility of the authors.

Financial support

This research was supported by the National Science Foundation (NSF) through Atmospheric and Geospace Sciences Grant No. 2232138. Computational resources were provided by UMBC's Chip High Performance Computing Facility.

References

Adams, A. M., Prospero, J. M., and Zhang, C.: CALIPSO-derived three-dimensional structure of aerosol over the Atlantic basin and adjacent continents, J. Climate, 25, 6862–6879, https://doi.org/10.1175/JCLI-D-11-00672.1, 2012.

https://doi.org/10.5194/egusphere-2026-4228
Preprint. Discussion started: 28 July 2026

Bauer, S. E. and Koch, D.: Impact of heterogeneous sulfate formation at mineral dust surfaces on aerosol loads and radiative forcing in the Goddard Institute for Space Studies general circulation model, J. Geophys. Res.-Atmos., 110, D17202, https://doi.org/10.1029/2005JD005870, 2005.

Bauer, S. E., Mishchenko, M. I., Lacis, A. A., Zhang, S., Perlwitz, J., and Metzger, S. M.: Do sulfate and nitrate coatings on mineral dust have important effects on radiative properties and climate modeling?, J. Geophys. Res.-Atmos., 112, D06307, https://doi.org/10.1029/2005JD006977, 2007.

Cwiertny, D. M., Young, M. A., and Grassian, V. H.: Chemistry and photochemistry of mineral dust aerosol, Annu. Rev. Phys. Chem., 59, 27–51, https://doi.org/10.1146/annurev.physchem.59.032607.093630, 2008.

Froyd, K. D., Murphy, D. M., Brock, C. A., Campuzano-Jost, P., Dibb, J. E., Jimenez, J.-L., Kupc, A., Middlebrook, A. M., Schill, G. P., Thornhill, K. L., Williamson, C. J., Wilson, J. C., and Ziemba, L. D.: A new method to quantify mineral dust and other aerosol species from aircraft platforms using single-particle mass spectrometry, Atmos. Meas. Tech., 12, 6209–6239, https://doi.org/10.5194/amt-12-6209-2019, 2019.

Hand, V. L., Capes, G., Vaughan, D. J., Formenti, P., Haywood, J. M., and Coe, H.: Evidence of internal mixing of African dust and biomass burning particles by individual particle analysis using electron beam techniques, J. Geophys. Res.-Atmos., 115, D13301, https://doi.org/10.1029/2009JD012938, 2010.

Huang, X., Chen, X., Zhou, D. K., and Liu, X.: An observationally based global band-by-band surface emissivity dataset for climate and weather simulations, J. Atmos. Sci., 73, 3541–3555, https://doi.org/10.1175/JAS-D-15-0355.1, 2016.

IPCC: Climate Change 2021: The Physical Science Basis. Contribution of Working Group I to the Sixth Assessment Report of the Intergovernmental Panel on Climate Change, edited by: Masson-Delmotte, V., Zhai, P., Pirani, A., Connors, S. L., Péan, C., Berger, S., Caud, N., Chen, Y., Goldfarb, L., Gomis, M. I., Huang, M., Leitzell, K., Lonnoy, E., Matthews, J. B. R., Maycock, T. K., Waterfield, T., Yelekçi, Ö., Yu, R., and Zhou, B., Cambridge University Press, Cambridge, UK and New York, NY, USA, 2391 pp., https://doi.org/10.1017/9781009157896, 2021.

https://doi.org/10.5194/egusphere-2026-4228
Preprint. Discussion started: 28 July 2026

Jordan, C. E., Dibb, J. E., Anderson, B. E., and Fuelberg, H. E.: Uptake of nitrate and sulfate on dust aerosols during TRACE-P, J. Geophys. Res.-Atmos., 108, 8817, https://doi.org/10.1029/2002JD003101, 2003.

Kim, M.-H., Omar, A. H., Tackett, J. L., Vaughan, M. A., Winker, D. M., Trepte, C. R., Hu, Y., Liu, Z., Poole, L. R., Pitts, M. C., Kar, J., and Magill, B. E.: The CALIPSO version 4 automated aerosol classification and lidar ratio selection algorithm, Atmos. Meas. Tech., 11, 6107–6135, https://doi.org/10.5194/amt-11-6107-2018, 2018.

Knippertz, P. and Stuut, J.-B. W. (Eds.): Mineral Dust: A Key Player in the Earth System, Springer, Dordrecht, the Netherlands, 509 pp., https://doi.org/10.1007/978-94-017-8978-3, 2014.

Kok, J. F., Storelvmo, T., Karydis, V. A., Adebiyi, A. A., Mahowald, N. M., Evan, A. T., He, C., and Leung, D. M.: Mineral dust aerosol impacts on global climate and climate change, Nat. Rev. Earth Environ., 4, 71–86, https://doi.org/10.1038/s43017-022-00379-5, 2023.

Krueger, B. J., Grassian, V. H., Cowin, J. P., and Laskin, A.: Heterogeneous chemistry of individual mineral dust particles from different dust source regions: The importance of particle mineralogy, Atmos. Environ., 38, 6253–6261, https://doi.org/10.1016/j.atmosenv.2004.07.010, 2004.

Li, W. J. and Shao, L. Y.: Observation of nitrate coatings on atmospheric mineral dust particles, Atmos. Chem. Phys., 9, 1863–1871, https://doi.org/10.5194/acp-9-1863-2009, 2009.

Li, W., Sun, J., Xu, L., Shi, Z., Riemer, N., Sun, Y., Fu, P., Zhang, J., Lin, Y., Wang, X., Shao, L., Chen, J., Zhang, X., Wang, Z., and Wang, W.: A conceptual framework for mixing structures in individual aerosol particles, J. Geophys. Res.-Atmos., 121, 13784–13798, https://doi.org/10.1002/2016JD025252, 2016.

Li, L., Mahowald, N. M., Obiso, V., Kok, J. F., Miller, R. L., Liu, X., Gonçalves Ageitos, M., Pérez García-Pando, C., Leung, D. M., Ke, Z., Brodrick, P. G., Clark, R. N., Formenti, P., Di Biagio, C., Ginoux, P., Okin, G. S., Zhou, B., Thompson, D. R., and Green, R. O.: Dust direct radiative effect including large particles and component minerals, Geophys. Res. Lett., 52, e2025GL119383, https://doi.org/10.1029/2025GL119383, 2025.

https://doi.org/10.5194/egusphere-2026-4228
Preprint. Discussion started: 28 July 2026

Omar, A. H., Winker, D. M., Vaughan, M. A., Hu, Y., Trepte, C. R., Ferrare, R. A., Lee, K.-P., Hostetler, C. A., Kittaka, C., Rogers, R. R., Kuehn, R. E., and Liu, Z.: The CALIPSO automated aerosol classification and lidar ratio selection algorithm, J. Atmos. Ocean. Tech., 26, 1994–2014, https://doi.org/10.1175/2009JTECHA1231.1, 2009.

Soussé Villa, R., Jorba, O., Gonçalves Ageitos, M., Bowdalo, D., Guevara, M., and Pérez García-Pando, C.: A comprehensive global modeling assessment of nitrate heterogeneous formation on desert dust, Atmos. Chem. Phys., 25, 4719–4753, https://doi.org/10.5194/acp-25-4719-2025, 2025.

Song, Q., Zhang, Z., Yu, H., Kato, S., Yang, P., Colarco, P., Remer, L. A., and Ryder, C. L.: Net radiative effects of dust in the tropical North Atlantic based on integrated satellite observations and in situ measurements, Atmos. Chem. Phys., 18, 11303–11322, https://doi.org/10.5194/acp-18-11303-2018, 2018.

Song, Q., Zhang, Z., Yu, H., Ginoux, P., and Shen, J.: Global dust optical depth climatology derived from CALIOP and MODIS aerosol retrievals on decadal timescales: Regional and interannual variability, Atmos. Chem. Phys., 21, 13369–13395, https://doi.org/10.5194/acp-21-13369-2021, 2021.

Song, Q., Zhang, Z., Yu, H., Kok, J. F., Di Biagio, C., Albani, S., Zheng, J., and Ding, J.: Size-resolved dust direct radiative effect efficiency derived from satellite observations, Atmos. Chem. Phys., 22, 13115–13135, https://doi.org/10.5194/acp-22-13115-2022, 2022.

Sumlin, B. J., Heinson, W. R., and Chakrabarty, R. K.: Retrieving the aerosol complex refractive index using PyMieScatt: A Mie computational package with visualization capabilities, J. Quant. Spectrosc. Ra., 205, 127–134, https://doi.org/10.1016/j.jqsrt.2017.10.012, 2018.

Taylor, M., Kazadzis, S., Amiridis, V., and Kahn, R. A.: Global aerosol mixtures and their multiyear and seasonal characteristics, Atmos. Environ., 116, 112–129, https://doi.org/10.1016/j.atmosenv.2015.06.029, 2015.

Teri, M., Gasteiger, J., Heimerl, K., Dollner, M., Schöberl, M., Seibert, P., Tipka, A., Müller, T., Aryasree, S., Kandler, K., and Weinzierl, B.: Pollution affects Arabian and Saharan dust optical properties in the eastern Mediterranean, Atmos. Chem. Phys., 25, 6633–6657, https://doi.org/10.5194/acp-25-6633-2025, 2025.

https://doi.org/10.5194/egusphere-2026-4228
Preprint. Discussion started: 28 July 2026

Tian, P., Zhang, L., Ma, J., Tang, K., Xu, L., Wang, Y., Cao, X., Liang, J., Ji, Y., Jiang, J. H., Yung, Y. L., and Zhang, R.: Radiative absorption enhancement of dust mixed with anthropogenic pollution over East Asia, Atmos. Chem. Phys., 18, 7815–7825, https://doi.org/10.5194/acp-18-7815-2018, 2018.

Unga, F., Choël, M., Derimian, Y., Deboudt, K., Riffault, V., Goloub, P., and Bernardoni, V.: Microscopic observations of core–shell particle structure and implications for atmospheric aerosol remote sensing, J. Geophys. Res.-Atmos., 123, 13944–13961, https://doi.org/10.1029/2018JD028602, 2018.

Xu, X., Yang, Y., Xiong, Z., Gong, J., and Luo, T.: Three-dimensional distribution and transport features of dust and polluted dust over China and surrounding areas from CALIPSO, Remote Sens., 15, 5734, https://doi.org/10.3390/rs15245734, 2023.

Yu, H., Kaufman, Y. J., Chin, M., Feingold, G., Remer, L. A., Anderson, T. L., Balkanski, Y., Bellouin, N., Boucher, O., Christopher, S., DeCola, P., Kahn, R., Koch, D., Loeb, N., Reddy, M. S., Schulz, M., Takemura, T., and Zhou, M.: A review of measurement-based assessments of the aerosol direct radiative effect and forcing, Atmos. Chem. Phys., 6, 613–666, https://doi.org/10.5194/acp-6-613-2006, 2006.

Zhang, Z., Song, Q., Zheng, J., and Yu, H.: Effects of surface coating on the shortwave and longwave radiative effects of dust aerosol in comparison with external mixing: A theoretical study, J. Quant. Spectrosc. Ra., 324, 109060, https://doi.org/10.1016/j.jqsrt.2024.109060, 2024.